

Electron correlation in 2D periodic systems

Oinam Romesh Meitei* and Troy Van Voorhis†

Department of Chemistry, Massachusetts Institute of Technology, Cambridge, MA 02139

(Dated: August 14, 2023)

Given the growing significance of 2D materials in various optoelectronic applications, it is imperative to have simulation tools that can accurately and efficiently describe electron correlation effects in these systems. Here, we show that the recently developed bootstrap embedding (BE) accurately predicts electron correlation energies and structural properties for 2D systems. Without explicit dependence on the reciprocal space sum (k -points) in the correlation calculation, BE can typically recover $\sim 99.5\%$ of the total electron correlation energy in 2D semi-metal, insulator and semiconductors. We demonstrate that BE can predict lattice constants and bulk moduli for 2D systems with high precision. Furthermore, we highlight the capability of BE to treat electron correlation in twisted bilayer graphene superlattices with large unit cells containing hundreds of carbon atoms. We find that as the twist angle decreases towards the magic angle, the correlation energy initially decreases in magnitude, followed by a subsequent increase. We conclude that BE is a promising electronic structure method for future applications to 2D materials.

I. INTRODUCTION

2D materials research has gained significant momentum in the past few years due to these materials' unique electronic, optical, and mechanical properties. These materials consist of a single layer of atoms or molecules arranged in a 2D lattice structure, which offers several advantages over their bulk counterparts. They exhibit exceptional mechanical, optical, and electrical properties, making them attractive for applications in various fields, including electronics¹, optoelectronics²⁻⁴, energy storage⁵, and catalysis^{6,1-4}. Notably, 2D materials have shown promising potential as topical insulators in electronic devices, as photocatalysts^{6,7}, and in organic light-emitting diodes (OLEDs)^{8,9}. Recently, the concept of twistronics, in which two or more layers of 2D materials are stacked at specific twist angles to create novel electronic states, has opened up new avenues for the application of 2D materials¹⁰⁻¹³. Such twisted layers of 2D materials have the potential to revolutionize the field of electronics¹⁴, quantum computing^{15,16}, superconductivity^{17,18}, and photonics^{19,20}.

Electron correlation effects play a crucial role in determining the electronic and optical properties of 2D materials. Unlike bulk materials, where electrons can move freely in three dimensions, 2D materials confine electrons in a reduced dimensionality, resulting in strong electron-electron interactions and reduced screening of Coulomb interactions. Only a handful of ab initio methods can treat electron correlation effects accurately in 2D systems, namely random phase approximation (RPA)^{21,22}, Moller-Plesset perturbation theory (MP2)^{23,24}, coupled cluster singles and doubles (CCSD)²⁵⁻²⁷, variational Monte Carlo (VMC)²⁸, and diffusion Monte Carlo²⁹. However, these methods are computationally demand-

ing and limited to small unit cells. Periodic quantum embedding methods offer a potential solution to the scalability of these methods by offering computations in sub-system space³⁰⁻⁴¹. Notable examples of periodic quantum embedding methods are the density functional embedding theory^{42,43}, projection-based wavefunction-in-DFT methods^{44,45}, density matrix embedding theory (DMET)⁴⁶⁻⁴⁹, ab initio DMFT⁵⁰, regional embedding⁵¹, and local embedding schemes⁵².

Alternatively, we have recently proposed periodic bootstrap embedding (BE) to treat electron correlation for periodic systems⁵³. The approach allows for a flexible partitioning of the system through the use of fragments with overlapping regions, and it has been shown to achieve convergence in the correlation energy as the fragment size increases. Furthermore, BE improves the embedding description by utilizing matching conditions in the overlapping region of the fragments⁵⁴⁻⁵⁸. Numerical tests have demonstrated the high accuracy of the method in computing electron correlation energy in 1D systems and its applicability to systems with large unit cell sizes. BE has also successfully treated electron correlation in molecules and supra-molecular complexes^{54,55,59}.

In this paper, we apply periodic BE to describe electron correlation in various 2D semiconducting materials that are important in diverse fields and applications, including energy storage, catalysis, electronics, optoelectronics, and photonics. Using only the mean-field computation at dense reciprocal space k -points, periodic BE provides access to correlation energy at the thermodynamic limit (TDL), which avoids finite-size effects at coarse k -points. Using CCSD as the choice of correlated solver, periodic BE-CCSD typically recovers $\sim 99.5\%$ of the electron correlation energy for the 2D systems tested in this work. Periodic BE-CCSD can effectively predict lattice constants and bulk moduli, which are important structural and mechanical properties of 2D systems. We further demonstrate the applicability of periodic BE to large periodic superlattice systems by computing correlation energies of twisted bilayer graphene at a twist angle

*Electronic address: oimeitei@mit.edu

†Electronic address: tvan@mit.edu

of 6.01° containing up to 364 carbon atoms in the elementary unit cell. The investigations on the 2D systems in this work are largely still a proof-of-concept, as they involve only computations with minimal basis sets. However, the results suggest the broad potential for periodic BE in electron correlation effects in 2D materials.

II. COMPUTATIONAL METHODS

A. Periodic Bootstrap Embedding

We begin by capturing the main ideas of periodic BE to treat electron correlation in 2D periodic systems⁵³. Consider partitioning a system into two distinct parts: a fragment comprising atom-centered localized orbitals and a bath encompassing the rest of the system. Due to the Schmidt decomposition technique, the many-body wavefunction of the entire system can be represented as a tensor product in the Hilbert space, consisting of the many-body fragment and the bath states:

$$|\Psi\rangle = \sum_p \lambda_p |f_p\rangle \otimes |b_p\rangle \quad (1)$$

with N_f being the number of fragment states, $|f_p\rangle$ and $|b_p\rangle$ the fragment and bath states, respectively, and λ_p characterizing the entanglement between the fragment and the bath. This expression considerably reduces the Hilbert space dimension of the system because the number of bath states cannot exceed the (much smaller) number of fragment states.

As the exact many-body wavefunction is not known a priori, BE employs an approximate bath constructed from the Hartree-Fock (HF) wavefunction instead of the actual many-body bath states to describe the embedding^{60,61}. When periodic boundary conditions are imposed, HF calculations are typically performed in reciprocal space to take advantage of the translational symmetries inherent in the system. Such computations are carried out on a grid of finite crystal momenta or k -point in the reciprocal space first Brillouin zone (FBZ). A transformation matrix $T^{k,A}$, composed of the coefficients of the fragment and the bath states, can then be utilized to derive the embedding Hamiltonian with the HF bath:

$$\hat{H}^A = \sum_{pq}^{2N_A} h_{pq}^A a_p^\dagger a_q + \frac{1}{2} \sum_{pqrs}^{2N_A} V_{pqrs}^A a_p^\dagger a_r^\dagger a_s a_q \quad (2)$$

with,

$$h_{pq}^A = \frac{1}{N_k} \sum_k \sum_{\mu\nu} T_{\mu p}^{k,A} F_{\mu\nu}^k T_{\nu q}^{k,A} - V_{pq}^{HF,A} \quad (3)$$

$$V_{pqrs}^A = \frac{1}{N_k} \sum_k \sum_{\mu\nu\lambda\sigma} T_{\mu p}^{k,A} T_{\nu q}^{k,A} V_{\mu\nu\lambda\sigma}^k T_{\lambda r}^{k,A} T_{\sigma s}^{k,A} \quad (4)$$

where F^k is the Fock matrix, V^k is the two-electron integrals, and $V^{HF,A}$ is the HF potential constructed using the HF density matrix in the embedding basis. Indices $\mu, \nu, \lambda, \sigma$ denote local orbitals (LOs) and p, q, r, s denote embedding orbitals. N_k is the total number of k -points, and N_A is the number of LOs in fragment A.

The above equations reveal that the fragment embedding Hamiltonian has no explicit dependence on the reciprocal space. As a result, \hat{H}^A can be solved with any non-periodic correlated electronic-structure method. This paper focuses on coupled cluster singles and doubles (CCSD) as the correlated fragment solver. Additionally, since the correlated fragment calculation does not rely on reciprocal space, approaching the thermodynamic limit (TDL) in an embedding calculation is relatively inexpensive; it is only necessary to converge the HF calculation to the TDL, and the correlated embedding calculation will also be converged⁵³.

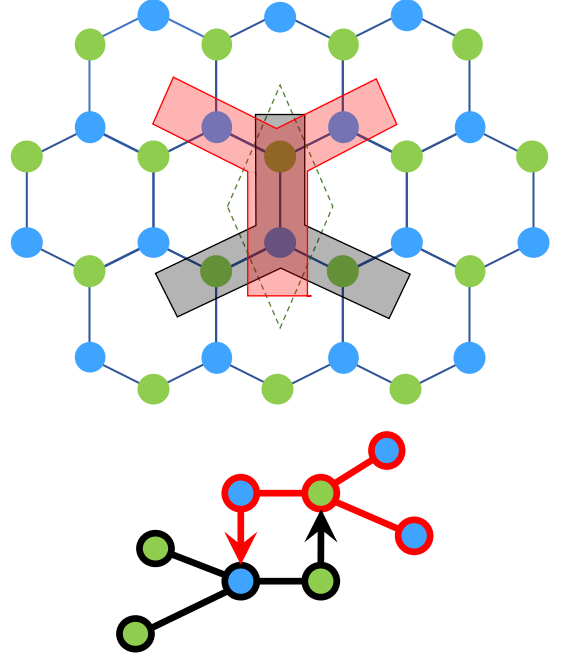


FIG. 1: Illustration of fragments in periodic BE in a hexagonal lattice system.

The embedding described above can be improved by partitioning the system into fragments that share an overlapped region⁵⁸. Figure 1 illustrates such a partitioning scheme for a hexagonal lattice system. The wavefunction at the center of each fragment in the overlapped region is described more accurately than the wavefunction at the edges of the fragment that are adjacent to the HF bath. The reason is that fragment edges more strongly interact with the HF bath compared to the fragment centers. By matching the wave function at the edge

of one fragment to the center of another fragment where they overlap, it is then possible to improve the embedding description. The matching of the wavefunction at the overlap region is accomplished in terms of the one-electron reduced density matrix (1-RDM) obtained from solving \hat{H}^A with CCSD method in this work. A global constraint is also imposed on the 1-RDM of each fragment center to conserve the total electron count.

Following our earlier works, we can systematically construct fragments with varying sizes by considering up to the second nearest connected atoms as the fragment edges^{54,56}. Henceforth, BE2 denotes fragments that include only the nearest neighboring atoms, and BE3 denotes fragments where the second nearest neighboring atoms are also included. By construction, the number of fragments equals the number of atoms in the unit-cell. For example, there are only two fragments in the honeycomb lattice shown in Figure 1 since the unit-cell contains only two atoms. When dealing with fragments where all edges extend outside the unit-cell, we construct a superlattice composed of (2×2) unit-cell to accommodate these fragments.

The total BE energy per unit cell is then computed as:

$$E = E_{HF} + \sum_A^{N_{frag}} \sum_{p \in C_A} \left[\sum_q^{2N_A} F_{pq}^{A,[0]} \Delta P_{pq}^A + \frac{1}{2} \sum_{qrs}^{2N_A} V_{pqrs}^A K_{pqrs}^A \right] \quad (5)$$

where E_{HF} is the HF energy, $F^{[0]}$ is the Fock matrix corresponding to the reference HF density in the embedding basis, ΔP^A is the difference in the correlated 1-RDM and the reference HF density of fragment A , and K^A is an approximate two-body cumulant as defined in Ref 62. We emphasize the significance of the energy expression in Equation 5 for achieving highly accurate correlation energy, in contrast to density-based energy expressions. In certain cases, employing the energy expression in Equation 5 has resulted in a reduction of correlation energy error from approximately 20% to less than 1% compared to the density-matrix-based energy used in, for example, refs. 46, 50, 54, 63, and 60.

B. Twist Averaging

To establish the accuracy of periodic BE for 2D systems, we compare BE total electron correlation energy per unit cell at the TDL to the full k -point CCSD method (hereafter denoted as k -CCSD). With the rapidly scaling cost of k -CCSD with respect to the system size (N^6) and k -points (N^4), computations were achievable only up to a limited number of k -points. The largest k -points that were used to compute k -CCSD correlation energy in this work was an 18x18 mesh for graphene. Large finite-size

errors are well known to occur at small k -points. To reduce the finite size error at the coarse k -points, the twist-averaging (TA) method was employed in this work to obtain the k -CCSD correlation energy⁶⁴⁻⁶⁸.

The TA method involves introducing a set of offsets, also called twist angles, to the unit cell of the crystal lattice. k -CCSD computations are then performed for each twist angle, and the resulting correlation energies are averaged over all the twist angles in this expression:

$$E_{corr}^{TA} = \frac{1}{N_s} \sum_{l=1}^{N_s} E_{corr}(k_s, l) \quad (6)$$

where N_s is the total number of twist angles, and $E_{corr}(k, l)$ is the k -CCSD correlation energy computed with the offset k_s .

Averaging the correlation energy over the twist angles enables an improved extrapolation to the thermodynamic limit, with a reduced finite size error for the coarse k -points. It should be noted that, due to the prohibitive scaling of k -CCSD with the number of k -points, each of the calculations performed for twist averaging at coarse k -points is much cheaper (often by orders of magnitude) than a calculation near the TDL. This effect is partially offset by the need to do several such calculations (typically around 30 in what follows) in order to converge the average. However, overall the improvement in accuracy is substantial. In some cases (most notably graphene) we are unable to extrapolate k -CCSD to the TDL without twist averaging. It should be noted that although the computational cost scales linearly with a factor of N_s , a significant number of k -CCSD calculations must be performed.

C. Calculation Details

The accuracy of periodic BE for 2D systems was tested on a set of monolayer 2D systems, namely graphene, hexagonal BN (h-BN), silicon carbide (SiC), triazine-based graphitic carbon nitride (g-C₃N₄), and molybdenum disulfide (MoS₂). Calculations were also performed on a set of twisted bilayer graphene. Further information on the structure of all the systems used in this work is provided in the Supporting Information.

All calculations reported in this work were carried out using a minimal basis set (STO-3G). The k -point HF and k -CCSF were performed with a Monkhorst-Pack k -point sampling. The BE calculations were performed with an in-house code that uses PySCF to generate the necessary integrals. To obtain the total correlation energy per unit cell at the TDL, a power law expansion was employed to extrapolate the BE and k -CCSD energies.

$$E(N_k) = E_\infty + \alpha N_k^{-1} \quad (7)$$

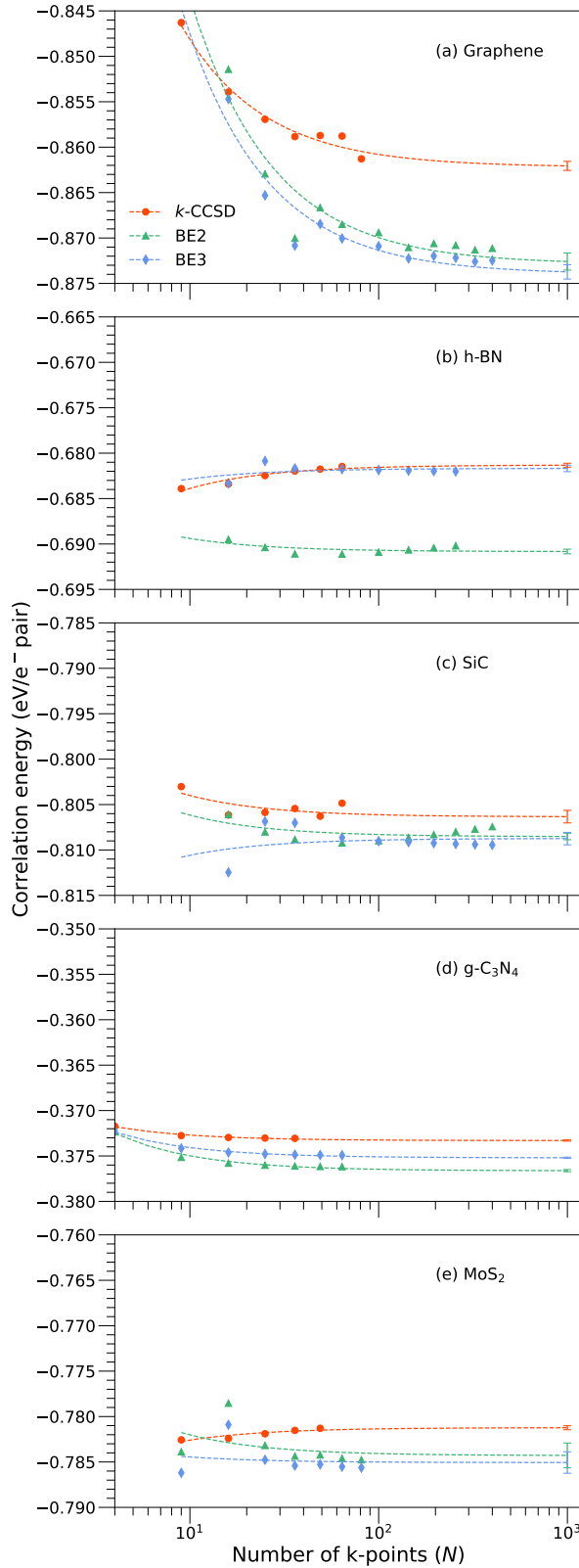


FIG. 2: Convergence of the total electron correlation energy to the thermodynamic limit with respect to k -points for 2D (a) Graphene, (b) h-BN, (c) SiC, (d) C₃N₄, and (e) MoS₂

III. RESULTS

A. Correlation Energies

First, we apply BE-CCSD to calculate total correlation energies per unit cell for a diverse set of five 2D systems: graphene, h-BN, SiC, g-C₃N₄, and MoS₂. Graphene is a widely recognized zero bandgap semi-metal with unique electronic and thermal properties^{69,70}. In contrast, h-BN, despite sharing the same honeycomb lattice structure with graphene, exhibits excellent insulating properties with a direct wide bandgap⁷¹. Additionally, the other 2D systems namely SiC, g-C₃N₄, and MoS₂, emerge as direct medium bandgap semiconductors^{72–74}. Apart from the electronic properties, these 2D systems exhibit high thermal and chemical stability, and are promising catalyst candidates^{73,75–77}. Notably, g-C₃N₄, has shown significant effectiveness as a photo-catalysts across a broad variety of reactions. In terms of dielectric constants, graphene stands out with the smallest value of 2.2, while the other 2D systems exhibit dielectric constants ranging from approximately 6 to 15. The dielectric constant as well as the band gaps of the 2D systems are listed in Table II.

TABLE I: Error at the thermodynamic limit. The total electron correlation energy per unit-cell from the BE2 and BE3 are compared to the full k -point CCSD correlation energy. Absolute errors are in meV/e⁻ pair

	BE2 error		BE3 error	
	Abs.	%	Abs.	%
Graphene	1.07±0.11	-1.2±0.1	1.18±0.09	-1.4±0.1
h-BN	0.95±0.03	-1.4±0.1	0.04±0.04	-0.1±0.1
SiC	0.22±0.08	-0.3±0.1	0.24±0.10	-0.3±0.1
g-C ₃ N ₄	0.32±0.11	-0.9±0.3	0.19±0.04	-0.5±0.1
MoS ₂	0.31±0.14	-0.4±0.2	0.38±0.12	-0.5±0.2

Table I presents the absolute and percentage error in the total electron correlation energy per unit cell at the TDL from BE2 and BE3 compared to the full k -CCSD energies. BE2 and BE3 reproduce the k -CCSD correlation with an error of $-1.2\pm0.1\%$ and $-1.4\pm0.1\%$, respectively, for graphene. Conversely, for h-BN, BE3 yields accurate electron correlation energy with an error of only $-0.1\pm0.1\%$ and BE2 with an error of $-1.4\pm0.1\%$. In the case of SiC, both BE2 and BE3 have an error of $-0.3\pm0.1\%$. For g-C₃N₄ and MoS₂, BE3 correlation energy has an error of -0.5% with an uncertainty of ±0.1 and ±0.2 , respectively, while BE2 results in an error of $-0.9\pm0.3\%$ and $-0.4\pm0.2\%$, respectively. Overall, the BE3 correlation energies are observed to be better (or in some cases similar) than the BE2 correlation energies. BE3 consistently achieves an accuracy of $\sim0.5\%$ (except for

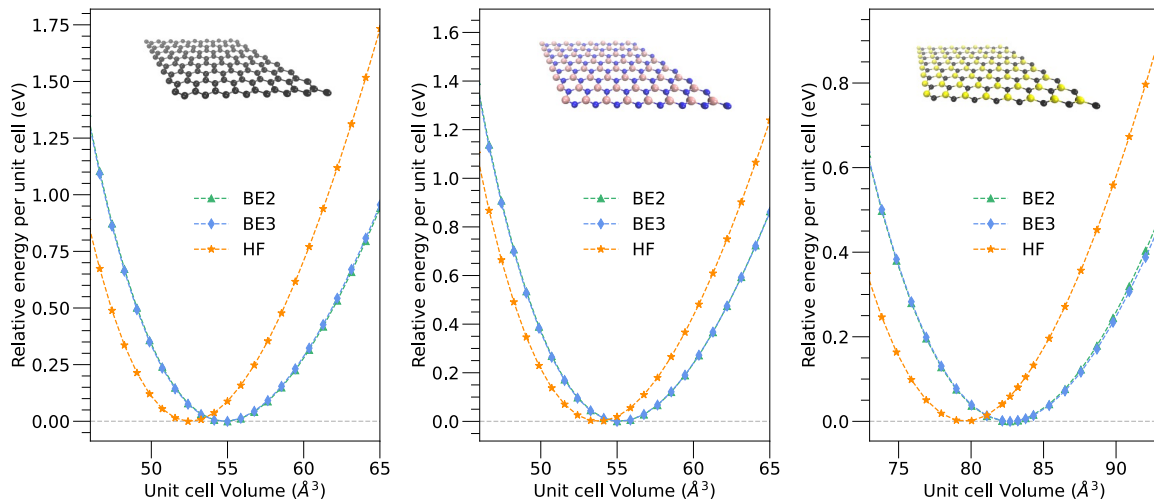


FIG. 3: Potential energy curves for graphene (left), h-BN (center), and SiC (right). The total energy per unit cell were computed using a k -mesh of (18×18) .

graphene), while the accuracy of BE2 shows less consistency, typically with an error of $\sim 1\%$.

The accuracy of BE3 correlates with the band-gap characteristics of the 2D systems. The corresponding band-gap values, along with the absolute errors of BE_n , are provided in Table II. Notably, BE3 almost exactly reproduce the full k -CCSD correlation energy for the h-BN, characterized by its wide band-gap. In contrast, the performance of BE3 is less accurate when applied to graphene which exhibits a zero band-gap. For 2D systems with intermediate band-gaps, specifically SiC, g-C₃N₄, and MoS₂, BE3 demonstrates a reasonable level of accuracy, falling between its performance on h-BN and graphene. Thus, BE3 yields accurate correlation energies for 2D systems characterized by medium to wide band-gaps, indicating that BE3 captures dynamic correlation more effectively compared to static correlation.

When considering dielectric constants of the 2D systems, there is no apparent correlation with the performance of BE_n . It is worth noting that graphene, which has the lowest dielectric constant among the 2D systems studied in this work, demonstrates the least accurate results. Conversely, BE3 is most accurate when applied to h-BN, which exhibits a dielectric constant of 6.83. In comparison, BE3 when applied to MoS₂, with a dielectric constant nearly twice that of h-BN, demonstrates an intermediate level of accuracy. The dielectric constant is associated with the range of correlation. However, given the lack of apparent dependence of the performance of BE_n on the dielectric constants and considering the sizes of the fragments for BE3, the range of correlation appears to have minimal influence on the performance of BE3.

Figure 2 plots the convergence of the total correlation energy per unit cell with respect to k -points computed with BE_n and k -CCSD for the different 2D systems, re-scaled per electron pair. Despite employing the TA method for k -CCSD, obtaining a smooth correlation en-

TABLE II: Band-gaps, dielectric constant and absolute errors of BE_n correlation energies in meV/e⁻ pair.

	Band-gap	Dielectric constant	Abs. error	
			BE2	BE3
Graphene	0.0 ⁶⁹	2.20 ⁷⁸	1.07	1.18
h-BN	5.9 ⁷¹	6.83 ⁷⁹	0.95	0.04
SiC	2.9 ⁷²	9.70 ⁸⁰	0.22	0.24
g-C ₃ N ₄	2.7 ⁷³	8.05 ⁸¹	0.32	0.19
MoS ₂	1.9 ⁷⁴	15.50 ⁷⁹	0.31	0.38

ergy extrapolation to the TDL is challenging for graphene and SiC. In particular, the slower convergence of correlation energy observed in graphene, coupled with the non-smooth extrapolation to the TDL, introduces uncertainties when using the extrapolated TDL correlation energy as a reference to assess the accuracy of BE_n . With more accurate k -CCSD correlation energy as a reference, it is plausible that these errors might be reduced. It is worth mentioning that correlation energy at extremely dense k -points, which are converged to the TDL can be computed with BE_n , as depicted in Figure 2. This eliminates the necessity for finite-size correction methods like TA in BE_n calculations.

B. Lattice Constants and Bulk Moduli

Having established the accuracy of periodic BE for correlation energies, we demonstrate applications of BE to obtain lattice constants and bulk moduli. Using a dense k -mesh of (18×18) and minimal basis, we computed the total energy per unit cell at varying unit cell volumes of

graphene, h-BN, and SiC. We then fit the results to a third-order Birch-Murnaghan equation-of-state⁸², shown in Figure 3, to obtain the bulk modulus, B_0 , and the lattice constant a_0 . We note that minimal basis set calculations presented here demonstrate that periodic BE can be used to predict structural properties at highly dense k -points, where it approaches convergence to the TDL. Such computations would be very challenging with the full k -CCSD for these systems.

TABLE III: Lattice constant a_0 , and bulk modulus B_0 of graphene, h-BN, and SiC.

	Graphene		h-BN		SiC	
	a_0	B_0	a_0	B_0	a_0	B_0
	(Å)	(GPa)	(Å)	(GPa)	(Å)	(GPa)
HF	2.46	265.54	2.49	231.02	3.03	167.57
BE2	2.52	215.36	2.52	207.57	3.09	143.07
BE3	2.52	216.30	2.52	206.24	3.09	140.51
Expt.	2.46 ⁸³		2.5 ⁸⁴		3.1 ⁸⁵	

Table III presents the lattice constants and bulk moduli obtained from HF and correlated BE_n calculations. Although the difference between the lattice constant values obtained from HF and BE_n may seem small, it is essential to note that electron correlation impacts the structural properties of these systems. This is especially noticeable in the bulk moduli, where the electron correlation effect is more pronounced. The BE_n lattice constants are insensitive to the fragment size. BE2 and BE3 results only differ by less than a tenth of a picometer. However, a slight difference is observed in the BE2 and BE3 results for bulk moduli. In the case of graphene, the lattice constant obtained from HF reproduces the experimental value⁸³, which is slightly different from the BE_n lattice constant. However, the comparison to experiment is challenging due to the small basis set. Different conclusions entirely might hold in a more realistic basis set. We have not pursued this further as the results here are only proof-of-concept. For h-BN, both HF and BE_n agree well with the experimental lattice constant⁸⁴. Finally, for SiC, the lattice constants obtained from BE_n differ by only a picometer from the experimental value⁸⁵. Overall, we observe that any errors associated with fragment size in BE_n are very smooth when comparing different geometries to one another - resulting in reliable and precise prediction of structural properties.

C. Twisted Bilayer Graphene

Twisted bilayer graphene (TBG) has recently gained significant attention due to its extraordinary elec-

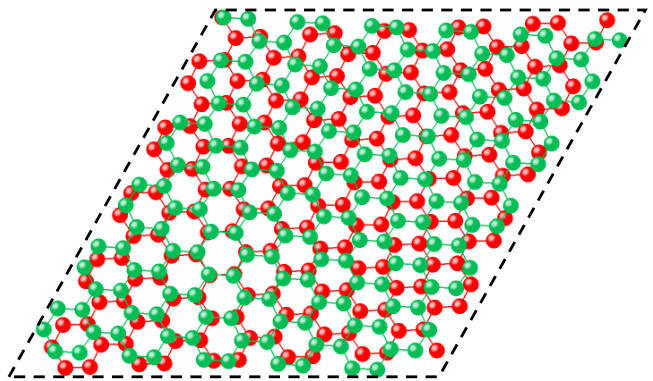


FIG. 4: Unit cell of twisted bilayer graphene superlattice with a twist angle of 6.01° . The stacked monolayers of graphene are shown in red and black. The unit cell of the superlattice contains 364 carbon atoms.

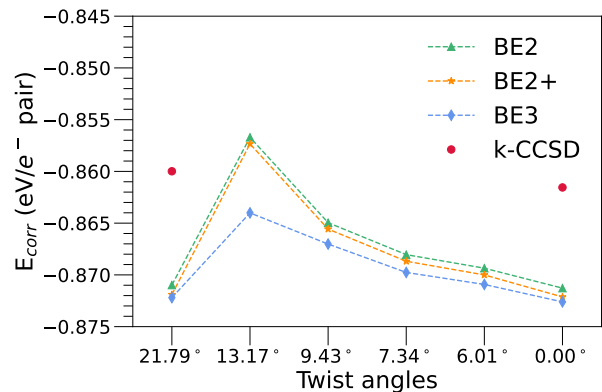


FIG. 5: Total correlation energy per unit cell computed with BE2, BE2+, and BE3 of the twisted bilayer graphene superlattice at different twist angles.

tronic properties resulting from a high periodicity moiré pattern^{10–12}. This fascinating material is created by stacking two graphene monolayers with a specific twisting angle, resulting in a unique electronic structure that can be tuned by adjusting the twist angle^{10,86}. The high periodicity moiré pattern observed in TBG leads to the emergence of new electronic states, including flat bands, which exhibit unique transport properties that make it a promising candidate for various electronic and optoelectronic applications^{87,88}. However, the honeycomb lattices of the two graphene monolayers only align to form periodic superlattices at certain discrete commensurate twist angles, and the elementary unit cell of the superlattices contains large number of carbon atoms^{10,89}. In particular, near the “magic angle” of 1.5° where exotic electronic states are observed⁸⁶, the commensurate supercells contain tens of thousands of carbon atoms. Even at relatively large twist angles, the number of atoms in the unit cell can be substantial. For instance, at approximately 6° twist angle, illustrated in Figure 4, the unit cell contains 364 atoms. Computations with such large unit cells are impossible with the full k -CCSD and challenging even at the Hartree-Fock level.

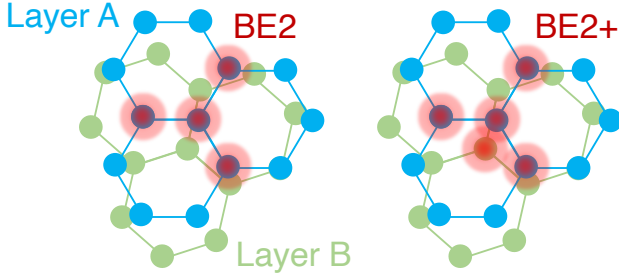


FIG. 6: Illustration of fragmentation schemes in bilayer graphene. BE_n fragment (left) comprises atoms from the same layer, while the $BE2+$ fragment (right) includes an additional atom from the adjacent layer.

We utilized BE_n to compute the total electron correlation energy of TBG at twist angles of 21.79° , 13.17° , 9.43° , 7.34° , and 6.01° . For twist angles smaller than 6° , the basic HF calculations became prohibitive with the PySCF periodic HF code we used to perform our calculations. With a more efficient HF implementation, we estimate the $BE2$ and $BE3$ calculations would be feasible down to approximately 3.48° , with a supercell size of 1084 atoms. Beyond that, the BE_n calculations would become disk-limited in performing the local integral transforms required for the fragment Hamiltonian. In addition to the BE_n fragment schemes, which consist of connected atoms, we introduce an additional fragment scheme called $BE2+$ (illustrated in Figure 6). This scheme incorporates an extra atom from the adjacent layer to capture the dispersion interactions between graphene layers. To achieve this, we employ a distance-based fragment scheme where we include the atom from the adjacent layer that is closest to the center of the $BE2$ fragment.

Figure 5 presents the total BE correlation energy per unit cell at the different twist angles including the untwisted bilayer graphene, normalized per electron pair. We also performed k -CCSD computations for the untwisted bilayer graphene (twist angle of 0°) and the twist angle of 21.79° employing the TA method. Because the k -CCSD computations were limited to coarse-grained k -points, we made comparisons for the BE_n energies computed at dense k -points to the k -CCSD energies at the coarse-grained k -points. Specifically, for the twist angle of 21.79° , the k -mesh was a 2×2 , while for the 0° twist angle, it was a 6×6 k -mesh in the k -CCSD calculations. For BE_n , the k -mesh was 6×6 and 18×18 for the twist angle of 21.79° and 0° , respectively. For the $21.79^\circ(0^\circ)$ twist angle, $BE2$, $BE2+$, and $BE3$ exhibited errors of $-1.3\%(-1.1\%)$, $-1.4\%(-1.3\%)$, and $-1.4\%(-1.2\%)$, respectively. The comparison of BE correlation energies to k -CCSD energies is limited due to finite size errors at the coarse-grained k -points and the computational scaling of k -CCSD. Nevertheless, we observe an unexpected physical phenomenon, where the correlation energy per electron pair initially decreases in magnitude before eventually increasing in the expected fashion as the twist an-

gle decreases toward the magic angle (where strong correlation effects can appear). It isn't entirely clear what leads to this effect, but it is interesting to note that it can only be accessed computationally using the tools presented here. k -CCSD is only computationally feasible for twist angles in the weak correlation regime where the correlation energy is decreasing with decreasing twist angle. Only with the improved BE_n hierarchy can one extend closer to the size regime where new physics can emerge.

IV. CONCLUSION

In conclusion, our study highlights the potential of periodic BE as a highly accurate electronic structure tool for studying 2D materials. Our $BE3$ fragment scheme with CCSD as the correlated fragment solver typically reproduces $\sim 99.5\%$ of the total electron correlation energy obtained from k -CCSD computations in 2D semimetal, insulator, and semiconductors. Notably, the correlated calculations in periodic BE are performed without the need for reciprocal space k -point sampling, which streamlines the computational efficiency. Our results demonstrate that BE offers reliable and precise prediction of lattice constants and bulk moduli for 2D systems. Particularly noteworthy is the capability of BE to generate smooth potential energy curves with respect to unit cell volumes at densely sampled k -points for 2D systems. Moreover, we demonstrate that $BE3$ can efficiently perform correlated calculations on twisted bilayer graphene superlattices with large unit cell sizes, with the only limiting factor being the HF calculations. The collective results presented herein demonstrate that periodic BE is a promising method with potential for future application in 2D materials. The accurate correlation energies derived from BE offer the means to calculate band-gaps through the computation of chemical potentials, as outlined in Ref. 90 and 91, which will be the objective of near future work. To enable realistic computations beyond the proof-of-concept minimal basis calculations, future efforts will also focus on developing BE for larger basis sets. Another direction for future work is enhancing the quantitative accuracy of the method for systems with narrow or gap-less band gaps, to improve the overall reliability of periodic BE.

Supplementary Information

Supplementary Information is provided for: (i) Distribution of correlation energy at the offsets in twist-averaging for k -CCSD; (ii) Geometric data including lattice constants and Cartesian coordinates.

Acknowledgments

This work was funded by a grant from NSF (NSF CHE-2154938).

- ¹ Zeng, M.; Xiao, Y.; Liu, J.; Yang, K.; Fu, L. Exploring Two-Dimensional Materials toward the Next-Generation Circuits: From Monomer Design to Assembly Control. *Chemical Reviews* **2018**, *118*, 6236–6296, PMID: 29381058.
- ² Momeni, K.; Ji, Y.; Wang, Y.; Paul, S.; Neshani, S.; Yilmaz, D. E.; Shin, Y. K.; Zhang, D.; Jiang, J.-W.; Park, H. S.; Sinnott, S.; van Duin, A.; Crespi, V.; Chen, L.-Q. Multiscale computational understanding and growth of 2D materials: a review. *npj Computational Materials* **2020**, *6*, 22.
- ³ Khan, K.; Tareen, A. K.; Aslam, M.; Wang, R.; Zhang, Y.; Mahmood, A.; Ouyang, Z.; Zhang, H.; Guo, Z. Recent developments in emerging two-dimensional materials and their applications. *J. Mater. Chem. C* **2020**, *8*, 387–440.
- ⁴ Novoselov, K. S.; Mishchenko, A.; Carvalho, A.; Neto, A. H. C. 2D materials and van der Waals heterostructures. *Science* **2016**, *353*, aac9439.
- ⁵ Wang, J.; Malgras, V.; Sugahara, Y.; Yamauchi, Y. Electrochemical energy storage performance of 2D nanoarchitected hybrid materials. *Nature Communications* **2021**, *12*, 3563.
- ⁶ Deng, D.; Novoselov, K. S.; Fu, Q.; Zheng, N.; Tian, Z.; Bao, X. Catalysis with two-dimensional materials and their heterostructures. *Nature Nanotechnology* **2016**, *11*, 218–230.
- ⁷ Zhao, Y.; Zhang, S.; Shi, R.; Waterhouse, G. I.; Tang, J.; Zhang, T. Two-dimensional photocatalyst design: A critical review of recent experimental and computational advances. *Materials Today* **2020**, *34*, 78–91.
- ⁸ Kim, M.; Ma, K. Y.; Kim, H.; Lee, Y.; Park, J. H.; Shin, H. S. 2D Materials in the Display Industry: Status and Prospects. *Advanced Materials* *n/a*, 2205520.
- ⁹ Zhang, L.; Sun, C.; He, T.; Jiang, Y.; Wei, J.; Huang, Y.; Yuan, M. High-performance quasi-2D perovskite light-emitting diodes: from materials to devices. *Light: Science & Applications* **2021**, *10*, 61.
- ¹⁰ Cao, Y.; Fatemi, V.; Fang, S.; Watanabe, K.; Taniguchi, T.; Kaxiras, E.; Jarillo-Herrero, P. Unconventional superconductivity in magic-angle graphene superlattices. *Nature* **2018**, *556*, 43–50.
- ¹¹ Cao, Y.; Fatemi, V.; Demir, A.; Fang, S.; Tomarken, S. L.; Luo, J. Y.; Sanchez-Yamagishi, J. D.; Watanabe, K.; Taniguchi, T.; Kaxiras, E.; Ashoori, R. C.; Jarillo-Herrero, P. Correlated insulator behaviour at half-filling in magic-angle graphene superlattices. *Nature* **2018**, *556*, 80–84.
- ¹² Andrei, E. Y.; MacDonald, A. H. Graphene bilayers with a twist. *Nature Materials* **2020**, *19*, 1265–1275.
- ¹³ Hennighausen, Z.; Kar, S. Twistronics: a turning point in 2D quantum materials. *Electronic Structure* **2021**, *3*, 014004.
- ¹⁴ Hennighausen, Z.; Kar, S. Twistronics: a turning point in 2D quantum materials. *Electronic Structure* **2021**, *3*, 014004.
- ¹⁵ Uri, A.; Grover, S.; Cao, Y.; Crosse, J. A.; Bagani, K.; Rodan Legrain, D.; Myasoedov, Y.; Watanabe, K.; Taniguchi, T.; Moon, P.; Koshino, M.; Jarillo Herrero, P.; Zeldov, E. Mapping the twist-angle disorder and Landau levels in magic-angle graphene. *Nature* **2020**, *581*, 47–52.
- ¹⁶ Cao, Y.; Rodan-Legrain, D.; Rubies-Bigorda, O.; Park, J. M.; Watanabe, K.; Taniguchi, T.; Jarillo-Herrero, P. Tunable correlated states and spin-polarized phases in twisted bilayer-bilayer graphene. *Nature* **2020**, *583*, 215–220.
- ¹⁷ Stepanov, P.; Das, I.; Lu, X.; Fahimniya, A.; Watanabe, K.; Taniguchi, T.; Koppens, F. H. L.; Lischner, J.; Levitov, L.; Efetov, D. K. Untying the insulating and superconducting orders in magic-angle graphene. *Nature* **2020**, *583*, 375–378.
- ¹⁸ Arora, H. S.; Polski, R.; Zhang, Y.; Thomson, A.; Choi, Y.; Kim, H.; Lin, Z.; Wilson, I. Z.; Xu, X.; Chu, J.-H.; Watanabe, K.; Taniguchi, T.; Alicea, J.; Nadj-Perge, S. Superconductivity in metallic twisted bilayer graphene stabilized by WSe₂. *Nature* **2020**, *583*, 379–384.
- ¹⁹ Tang, H.; Du, F.; Carr, S.; DeVault, C.; Mello, O.; Mazur, E. Modeling the optical properties of twisted bilayer photonic crystals. *Light: Science & Applications* **2021**, *10*, 157.
- ²⁰ Chen, J.; Lin, X.; Chen, M.; Low, T.; Chen, H.; Dai, S. A perspective of twisted photonic structures. *Applied Physics Letters* **2021**, *119*, 240501.
- ²¹ Harl, J.; Kresse, G. Accurate Bulk Properties from Approximate Many-Body Techniques. *Phys. Rev. Lett.* **2009**, *103*, 056401.
- ²² Harl, J.; Schimka, L.; Kresse, G. Assessing the quality of the random phase approximation for lattice constants and atomization energies of solids. *Phys. Rev. B* **2010**, *81*, 115126.
- ²³ Hirata, S.; Grabowski, I.; Tobita, M.; Bartlett, R. J. Highly accurate treatment of electron correlation in polymers: coupled-cluster and many-body perturbation theories. *Chemical Physics Letters* **2001**, *345*, 475–480.
- ²⁴ Ayala, P. Y.; Kudin, K. N.; Scuseria, G. E. Atomic orbital Laplace-transformed second-order Møller–Plesset theory for periodic systems. *The Journal of Chemical Physics* **2001**, *115*, 9698–9707.
- ²⁵ Katagiri, H. Equation-of-motion coupled-cluster study on exciton states of polyethylene with periodic boundary condition. *The Journal of Chemical Physics* **2005**, *122*, 224901.
- ²⁶ Grüneis, A.; Booth, G. H.; Marsman, M.; Spencer, J.; Alavi, A.; Kresse, G. Natural Orbitals for Wave Function Based Correlated Calculations Using a Plane Wave Basis Set. *Journal of Chemical Theory and Computation* **2011**, *7*, 2780–2785, PMID: 26605469.
- ²⁷ McClain, J.; Sun, Q.; Chan, G. K.-L.; Berkelbach, T. C. Gaussian-Based Coupled-Cluster Theory for the Ground-State and Band Structure of Solids. *Journal of Chemical Theory and Computation* **2017**, *13*, 1209–1218, PMID:

- 28218843.
- 28 Giamarchi, T.; Lhuillier, C. Phase diagrams of the two-dimensional Hubbard and t-J models by a variational Monte Carlo method. *Phys. Rev. B* **1991**, *43*, 12943–12951.
 - 29 Foulkes, W. M. C.; Mitas, L.; Needs, R. J.; Rajagopal, G. Quantum Monte Carlo simulations of solids. *Rev. Mod. Phys.* **2001**, *73*, 33–83.
 - 30 Danyliv, O.; Kantorovich, L.; Corá, F. Treating periodic systems using embedding: Adams-Gilbert approach. *Phys. Rev. B* **2007**, *76*, 045107.
 - 31 Doblhoff-Dier, K.; Kroes, G.-J.; Libisch, F. Density functional embedding for periodic and nonperiodic diffusion Monte Carlo calculations. *Phys. Rev. B* **2018**, *98*, 085138.
 - 32 Tölle, J.; Severo Pereira Gomes, A.; Ramos, P.; Pavanello, M. Charged-cell periodic DFT simulations via an impurity model based on density embedding: Application to the ionization potential of liquid water. *International Journal of Quantum Chemistry* **2019**, *119*, e25801.
 - 33 Lubert, S. Local electric dipole moments for periodic systems via density functional theory embedding. *The Journal of Chemical Physics* **2014**, *141*, 234110.
 - 34 Rusakov, A. A.; Iskakov, S.; Tran, L. N.; Zgid, D. Self-Energy Embedding Theory (SEET) for Periodic Systems. *Journal of Chemical Theory and Computation* **2019**, *15*, 229–240, PMID: 30540474.
 - 35 Christlmaier, E. M.; Kats, D.; Alavi, A.; Usvyat, D. Full configuration interaction quantum Monte Carlo treatment of fragments embedded in a periodic mean field. *The Journal of Chemical Physics* **2022**, *156*, 154107.
 - 36 Pascual, J. L.; Seijo, L. Ab initio model potential embedded cluster calculations including lattice relaxation and polarization: Local distortions on Mn²⁺-doped CaF₂. *The Journal of Chemical Physics* **1995**, *102*, 5368–5376.
 - 37 Lin, H.-H.; Maschio, L.; Kats, D.; Usvyat, D.; Heine, T. Fragment-Based Restricted Active Space Configuration Interaction with Second-Order Corrections Embedded in Periodic Hartree–Fock Wave Function. *Journal of Chemical Theory and Computation* **2020**, *16*, 7100–7108, PMID: 33074688.
 - 38 Masur, O.; Schütz, M.; Maschio, L.; Usvyat, D. Fragment-Based Direct-Local-Ring-Coupled-Cluster Doubles Treatment Embedded in the Periodic Hartree–Fock Solution. *Journal of Chemical Theory and Computation* **2016**, *12*, 5145–5156, PMID: 27556287.
 - 39 Usvyat, D.; Maschio, L.; Schutz, M. Periodic and fragment models based on the local correlation approach. *WIREs Computational Molecular Science* **2018**, *8*, e1357.
 - 40 Pisani, C.; Dovesi, R.; Carosso, P. Moderately-large-embedded-cluster approach to the study of local defects in solids. Vacancy and substitutional impurities in graphite. *Phys. Rev. B* **1979**, *20*, 5345–5357.
 - 41 Inglesfield, J. Embedding at surfaces. *Computer Physics Communications* **2001**, *137*, 89–107.
 - 42 Govind, N.; Wang, Y.; da Silva, A.; Carter, E. Accurate ab initio energetics of extended systems via explicit correlation embedded in a density functional environment. *Chemical Physics Letters* **1998**, *295*, 129–134.
 - 43 Klüner, T.; Govind, N.; Wang, Y. A.; Carter, E. A. Periodic density functional embedding theory for complete active space self-consistent field and configuration interaction calculations: Ground and excited states. *The Journal of Chemical Physics* **2002**, *116*, 42–54.
 - 44 Chulhai, D. V.; Goodpaster, J. D. Projection-Based Correlated Wave Function in Density Functional Theory Embedding for Periodic Systems. *Journal of Chemical Theory and Computation* **2018**, *14*, 1928–1942, PMID: 29494155.
 - 45 Petras, H. R.; Graham, D. S.; Ramadugu, S. K.; Goodpaster, J. D.; Shepherd, J. J. Fully Quantum Embedding with Density Functional Theory for Full Configuration Interaction Quantum Monte Carlo. *Journal of Chemical Theory and Computation* **2019**, *15*, 5332–5342, PMID: 31449406.
 - 46 Bulik, I. W.; Chen, W.; Scuseria, G. E. Electron correlation in solids via density embedding theory. *The Journal of Chemical Physics* **2014**, *141*, 054113.
 - 47 Cui, Z.-H.; Zhu, T.; Chan, G. K.-L. Efficient Implementation of Ab Initio Quantum Embedding in Periodic Systems: Density Matrix Embedding Theory. *Journal of Chemical Theory and Computation* **2020**, *16*, 119–129.
 - 48 Pham, H. Q.; Hermes, M. R.; Gagliardi, L. Periodic Electronic Structure Calculations with the Density Matrix Embedding Theory. *Journal of Chemical Theory and Computation* **2020**, *16*, 130–140, PMID: 31815455.
 - 49 Mitra, A.; Pham, H. Q.; Pandharkar, R.; Hermes, M. R.; Gagliardi, L. Excited States of Crystalline Point Defects with Multireference Density Matrix Embedding Theory. *The Journal of Physical Chemistry Letters* **2021**, *12*, 11688–11694, PMID: 34843250.
 - 50 Zhu, T.; Cui, Z.-H.; Chan, G. K.-L. Efficient Formulation of Ab Initio Quantum Embedding in Periodic Systems: Dynamical Mean-Field Theory. *Journal of Chemical Theory and Computation* **2020**, *16*, 141–153, PMID: 31815457.
 - 51 Lau, B. T. G.; Knizia, G.; Berkelbach, T. C. Regional Embedding Enables High-Level Quantum Chemistry for Surface Science. *The Journal of Physical Chemistry Letters* **2021**, *12*, 1104–1109, PMID: 33475362.
 - 52 Schäfer, T.; Libisch, F.; Kresse, G.; Grüneis, A. Local embedding of coupled cluster theory into the random phase approximation using plane waves. *The Journal of Chemical Physics* **2021**, *154*, 011101.
 - 53 Meitei, O. R.; Van Voorhis, T. Periodic Bootstrap Embedding. *arXiv:2301.06153* **2023**.
 - 54 Ye, H.-Z.; Tran, H. K.; Van Voorhis, T. Bootstrap Embedding For Large Molecular Systems. *Journal of Chemical Theory and Computation* **2020**, *16*, 5035–5046.
 - 55 Ye, H.-Z.; Rieke, N. D.; Tran, H. K.; Van Voorhis, T. Bootstrap Embedding for Molecules. *Journal of Chemical Theory and Computation* **2019**, *15*, 4497–4506, PMID: 31343878.
 - 56 Ye, H.-Z.; Van Voorhis, T. Atom-Based Bootstrap Embedding For Molecules. *The Journal of Physical Chemistry Letters* **2019**, *10*, 6368–6374, PMID: 31578867.
 - 57 Tran, H. K.; Ye, H.-Z.; Van Voorhis, T. Bootstrap embedding with an unrestricted mean-field bath. *The Journal of Chemical Physics* **2020**, *153*, 214101.
 - 58 Welborn, M.; Tsuchimochi, T.; Van Voorhis, T. Bootstrap embedding: An internally consistent fragment-based method. *The Journal of Chemical Physics* **2016**, *145*, 074102.
 - 59 Rieke, N.; Welborn, M.; Ye, H.-Z.; Voorhis, T. V. Performance of Bootstrap Embedding for long-range interactions and 2D systems. *Molecular Physics* **2017**, *115*, 2242–2253.
 - 60 Knizia, G.; Chan, G. K.-L. Density Matrix Embedding: A Strong-Coupling Quantum Embedding Theory. *Journal of Chemical Theory and Computation* **2013**, *9*, 1428–1432, PMID: 26587604.

- ⁶¹ Knizia, G.; Chan, G. K.-L. Density Matrix Embedding: A Simple Alternative to Dynamical Mean-Field Theory. *Phys. Rev. Lett.* **2012**, *109*, 186404.
- ⁶² Nusspickel, M.; Ibrahim, B.; Booth, G. H. On the effective reconstruction of expectation values from ab initio quantum embedding. *arXiv:2210.14561* **2022**,
- ⁶³ Knizia, G. Intrinsic Atomic Orbitals: An Unbiased Bridge between Quantum Theory and Chemical Concepts. *Journal of Chemical Theory and Computation* **2013**, *9*, 4834–4843, PMID: 26583402.
- ⁶⁴ Lin, C.; Zong, F. H.; Ceperley, D. M. Twist-averaged boundary conditions in continuum quantum Monte Carlo algorithms. *Phys. Rev. E* **2001**, *64*, 016702.
- ⁶⁵ Mihm, T. N.; McIsaac, A. R.; Shepherd, J. J. An optimized twist angle to find the twist-averaged correlation energy applied to the uniform electron gas. *The Journal of Chemical Physics* **2019**, *150*, 191101.
- ⁶⁶ Mihm, T. N.; Schäfer, T.; Ramadugu, S. K.; Weiler, L.; Grüneis, A.; Shepherd, J. J. A shortcut to the thermodynamic limit for quantum many-body calculations of metals. *Nature Computational Science* **2021**, *1*.
- ⁶⁷ Gruber, T.; Liao, K.; Tsatsoulis, T.; Hummel, F.; Grüneis, A. Applying the Coupled-Cluster Ansatz to Solids and Surfaces in the Thermodynamic Limit. *Phys. Rev. X* **2018**, *8*, 021043.
- ⁶⁸ Liao, K.; Grüneis, A. Communication: Finite size correction in periodic coupled cluster theory calculations of solids. *The Journal of Chemical Physics* **2016**, *145*, 141102.
- ⁶⁹ Novoselov, K. S.; Falko, V. I.; Colombo, L.; Gellert, P. R.; Schwab, M. G.; Kim, K. A roadmap for graphene. *Nature* **2012**, *490*, 192–200.
- ⁷⁰ Brandenburg, J. G.; Zen, A.; Fitzner, M.; Ramberger, B.; Kresse, G.; Tsatsoulis, T.; Grüneis, A.; Michaelides, A.; Alfè, D. Physisorption of Water on Graphene: Subchemical Accuracy from Many-Body Electronic Structure Methods. *The Journal of Physical Chemistry Letters* **2019**, *10*, 358–368.
- ⁷¹ Cassabois, G.; Valvin, P.; Gil, B. Hexagonal boron nitride is an indirect bandgap semiconductor. *Nature Photonics* **2016**, *10*, 262–266.
- ⁷² Hoat, D.; Naseri, M.; Hieu, N. N.; Ponce-Pérez, R.; Rivas-Silva, J.; Coccoletzi, G. H. Transition from indirect to direct band gap in SiC monolayer by chemical functionalization: A first principles study. *Superlattices and Microstructures* **2020**, *137*, 106320.
- ⁷³ Zhu, B.; Xia, P.; Li, Y.; Ho, W.; Yu, J. Fabrication and photocatalytic activity enhanced mechanism of direct Z-scheme g-C₃N₄/Ag₂WO₄ photocatalyst. *Applied Surface Science* **2017**, *391*, 175–183, 2nd International Symposium on Energy and Environmental Photocatalytic Materials.
- ⁷⁴ Mak, K. F.; Lee, C.; Hone, J.; Shan, J.; Heinz, T. F. Atomically Thin MoS₂: A New Direct-Gap Semiconductor. *Phys. Rev. Lett.* **2010**, *105*, 136805.
- ⁷⁵ Aïssa, B.; Memon, N. K.; Ali, A.; Khraisheh, M. K. Recent Progress in the Growth and Applications of Graphene as a Smart Material: A Review. *Frontiers in Materials* **2015**, *2*.
- ⁷⁶ Sahu, S.; Rout, G. C. Band gap opening in graphene: a short theoretical study. *International Nano Letters* **2017**, *7*, 81–89.
- ⁷⁷ Moon, S.; Kim, J.; Park, J.; Im, S.; Kim, J.; Hwang, I.; Kim, J. K. Hexagonal Boron Nitride for Next-Generation Photonics and Electronics. *Advanced Materials* **2023**, *35*, 2204161.
- ⁷⁸ Elias, D. C.; Gorbachev, R. V.; Mayorov, A. S.; Morozov, S. V.; Zhukov, A. A.; Blake, P.; Ponomarenko, L. A.; Grigorieva, I. V.; Novoselov, K. S.; Guinea, F.; Geim, A. K. Dirac cones reshaped by interaction effects in suspended graphene. *Nature Physics* **2011**, *7*, 701–704.
- ⁷⁹ Laturia, A.; Van de Put, M. L.; Vandenbergh, W. G. Dielectric properties of hexagonal boron nitride and transition metal dichalcogenides: from monolayer to bulk. *npj 2D Materials and Applications* **2018**, *2*, 6.
- ⁸⁰ Liu, Y.; Fang, Y.; Yang, D.; Pi, X.; Wang, P. Recent progress of heterostructures based on two dimensional materials and wide bandgap semiconductors. *Journal of Physics: Condensed Matter* **2022**, *34*, 183001.
- ⁸¹ Patra, P. C.; Mohapatra, Y. N. Dielectric constant of thin film graphitic carbon nitride (g-C₃N₄) and double dielectric Al₂O₃/g-C₃N₄. *Applied Physics Letters* **2021**, *118*, 103501.
- ⁸² Birch, F. Finite Elastic Strain of Cubic Crystals. *Phys. Rev.* **1947**, *71*, 809–824.
- ⁸³ Ferrari, A. C.; Meyer, J. C.; Scardaci, V.; Casiraghi, C.; Lazzeri, M.; Mauri, F.; Piscanec, S.; Jiang, D.; Novoselov, K. S.; Roth, S.; Geim, A. K. Raman Spectrum of Graphene and Graphene Layers. *Phys. Rev. Lett.* **2006**, *97*, 187401.
- ⁸⁴ Pakdel, A.; Bando, Y.; Golberg, D. Nano boron nitride flatland. *Chem. Soc. Rev.* **2014**, *43*, 934–959.
- ⁸⁵ Chabi, S.; Guler, Z.; Brearley, A. J.; Benavidez, A. D.; Luk, T. S. The Creation of True Two-Dimensional Silicon Carbide. *Nanomaterials* **2021**, *11*.
- ⁸⁶ Yankowitz, M.; Chen, S.; Polshyn, H.; Zhang, Y.; Watanabe, K.; Taniguchi, T.; Graf, D.; Young, A. F.; Dean, C. R. Tuning superconductivity in twisted bilayer graphene. *Science* **2019**, *363*, 1059–1064.
- ⁸⁷ Nimbalkar, A.; Kim, H. Opportunities and Challenges in Twisted Bilayer Graphene: A Review. *Nano-Micro Letters* **2020**, *12*, 126.
- ⁸⁸ Tiutiunnyk, A.; Duque, C.; Caro-Lopera, F.; Mora-Ramos, M.; Correa, J. Opto-electronic properties of twisted bilayer graphene quantum dots. *Physica E: Low-dimensional Systems and Nanostructures* **2019**, *112*, 36–48.
- ⁸⁹ Bistrizter, R.; MacDonald, A. H. Moiré bands in twisted double-layer graphene. *Proceedings of the National Academy of Sciences* **2011**, *108*, 12233–12237.
- ⁹⁰ Helbig, N.; Lathiotakis, N. N.; Gross, E. K. U. Discontinuity of the chemical potential in reduced-density-matrix-functional theory for open-shell systems. *Phys. Rev. A* **2009**, *79*, 022504.
- ⁹¹ Perdew, J. P.; Parr, R. G.; Levy, M.; Balduz, J. L. Density-Functional Theory for Fractional Particle Number: Derivative Discontinuities of the Energy. *Phys. Rev. Lett.* **1982**, *49*, 1691–1694.